Check for updates

Received: 11 July 2022 | Revised: 10 October 2022 | Accepted: 17 October 2022
DOI: 10.1002/glia.24290

GLIA
WILEY

RESEARCH ARTICLE

Focused ion beam-scanning electron microscopy links pathological myelin outfoldings to axonal changes in mice lacking *Plp1* or *Mag*

Anna M. Steyer[1,2] | Tobias J. Buscham[1] | Charlotta Lorenz[3] | Sophie Hümmert[1] | Maria A. Eichel-Vogel[1] | Leonie C. Schadt[1] | Julia M. Edgar[1,4] | Sarah Köster[3,5] | Wiebke Möbius[1,2,5] | Klaus-Armin Nave[1] | Hauke B. Werner[1]

[1]Department of Neurogenetics, Max Planck Institute for Multidisciplinary Sciences, Göttingen, Germany

[2]Electron Microscopy-City Campus, Max Planck Institute for Multidisciplinary Sciences, Göttingen, Germany

[3]Institute for X-Ray Physics, University of Göttingen, Göttingen, Germany

[4]Institute of Infection, Immunity and Inflammation, College of Medical, Veterinary and Life Sciences, University of Glasgow, Glasgow, UK

[5]Cluster of Excellence 'Multiscale Bioimaging: from Molecular Machines to Networks of Excitable Cells' (MBExC), University of Göttingen, Göttingen, Germany

Correspondence
Hauke Werner, Department of Neurogenetics, Max Planck Institute for Multidisciplinary Sciences, Hermann Rein Str. 3, D-37075 Göttingen, Germany.
Email: hauke@mpinat.mpg.de

Funding information
Deutsche Forschungsgemeinschaft, Grant/Award Number: WE 2720/2-2 to HBW

Abstract

Healthy myelin sheaths consist of multiple compacted membrane layers closely encasing the underlying axon. The ultrastructure of CNS myelin requires specialized structural myelin proteins, including the transmembrane-tetraspan proteolipid protein (PLP) and the Ig-CAM myelin-associated glycoprotein (MAG). To better understand their functional relevance, we asked to what extent the axon/myelin-units display similar morphological changes if PLP or MAG are lacking. We thus used focused ion beam-scanning electron microscopy (FIB-SEM) to re-investigate axon/myelin-units side-by-side in *Plp*- and *Mag*-null mutant mice. By three-dimensional reconstruction and morphometric analyses, pathological myelin outfoldings extend up to 10 μm longitudinally along myelinated axons in both models. More than half of all assessed outfoldings emerge from internodal myelin. Unexpectedly, three-dimensional reconstructions demonstrated that both models displayed complex axonal pathology underneath the myelin outfoldings, including axonal sprouting. Axonal anastomosing was additionally observed in *Plp*-null mutant mice. Importantly, normal-appearing axon/myelin-units displayed significantly increased axonal diameters in both models according to quantitative assessment of electron micrographs. These results imply that healthy CNS myelin sheaths facilitate normal axonal diameters and shape, a function that is impaired when structural myelin proteins PLP or MAG are lacking.

Anna M. Steyer and Tobias J. Buscham contributed equally to this study.

This is an open access article under the terms of the Creative Commons Attribution License, which permits use, distribution and reproduction in any medium, provided the original work is properly cited.
© 2022 The Authors. *GLIA* published by Wiley Periodicals LLC.

10981136, 2023, 3, Downloaded from https://onlinelibrary.wiley.com/doi/10.1002/glia.24290 by University Of Glasgow, Wiley Online Library on [24/01/2023]. See the Terms and Conditions (https://onlinelibrary.wiley.com/terms-and-conditions) on Wiley Online Library for rules of use; OA articles are governed by the applicable Creative Commons License

KEYWORDS
anastomosed axons, axonal diameter, axonal sprouting, axon-glia interaction, focused ion beam-scanning electron microscopy (FIB-SEM), myelin outfoldings, myelin sheath, neuropathology, oligodendrocyte, spastic paraplegia (SPG)

1 | INTRODUCTION

Fast-conducting vertebrate axons are closely encased by myelin sheaths, which insulate the long internodal axonal segments between the nodes of Ranvier (Hartline & Colman, 2007). In the central nervous system (CNS), oligodendrocytes provide both the multilayered myelin sheaths and metabolic support to axons (Nave & Werner, 2014; Philips & Rothstein, 2017). Myelin is required for normal motor, sensory and cognitive abilities, as demonstrated by functional decline in human patients with myelin-related disorders and respective animal models (Stadelmann et al., 2019; Wolf et al., 2020).

The development and maintenance of the normal ultrastructure of CNS myelin requires specialized structural myelin proteins, including the most abundant protein of compact myelin (Gargareta et al., 2022; Jahn et al., 2020), the cholesterol-associated transmembrane-tetraspan proteolipid protein (PLP), and myelin-associated glycoprotein (MAG), a single-span transmembrane protein that exposes five Immunoglobulin-like (Ig-like) domains from the adaxonal myelin surface to the underlying axon (McKerracher & Rosen, 2015; Myllykoski et al., 2018; Nave & Werner, 2014). The functional relevance of PLP and MAG in vivo is commonly assessed in *Plp*$^{-/Y}$ (Gould et al., 2018; Griffiths et al., 1998) and *Mag*$^{-/-}$ mutant mice (Li et al., 1994; Montag et al., 1994).

Plp$^{-/Y}$ and *Mag*$^{-/-}$ mice share pathological features including moderate CNS hypomyelination (Bartsch et al., 1997; De Monasterio-Schrader et al., 2013; Li et al., 1998; Yool et al., 2001). However, each model also displays distinct pathology of the axon/myelin-unit such as axonal swellings in *Plp*$^{-/Y}$ mice (Edgar et al., 2004; Griffiths et al., 1998) and impaired integrity of the axon/myelin apposition in *Mag*$^{-/-}$ mice (Li et al., 1994; Marcus et al., 2002; Montag et al., 1994). More recently, we found that both mutants develop pathological outfoldings of their myelin sheaths (Patzig, Erwig, et al., 2016), a feature that was previously reported in *Mag*$^{-/-}$ mice (Biffiger et al., 2000; Li et al., 1994, 1998) but to the best of our knowledge not in *Plp*$^{-/Y}$ mice. These findings (Patzig, Erwig, et al., 2016) indicate that morphological assessment in multiple mouse models side-by-side can identify pathological features that were previously overlooked in individual characterizations.

Previous morphological assessment of these mutants was largely based on conventional transmission electron microscopy (TEM), which lacks the third dimension and therefore allows only limited visualization of axon/myelin units. For example, TEM yields only incomplete information about the shape and dimensions of myelin outfoldings. It thus remains unknown if outfoldings emerge from the internodal or paranodal segments of the myelin sheath in the pathological CNS. Notwithstanding that myelin outfoldings are a common pathological feature in several other myelin mutants (Erwig et al., 2019; Katanov et al., 2020; Patzig, Erwig, et al., 2016), as well as in the normal developing (Cullen & Webster, 1979; Djannatian et al., 2021; Patzig, Erwig, et al., 2016; Snaidero et al., 2014) and aging CNS (Bowley et al., 2010; Hill et al., 2018; Peters, 2002; Sturrock, 1976), our knowledge about this neuropathological feature has thus remained limited.

Here, we assessed myelin outfoldings in the CNS of *Plp*$^{-/Y}$ and *Mag*$^{-/-}$ mice using focused ion beam-scanning electron microscopy (FIB-SEM), which allows three-dimensional reconstruction of axon/myelin-units. We find that myelin outfoldings are large sheets of multimembrane stacks that longitudinally extend up to 10 μm along myelinated axons. Over half of all assessed outfoldings emerged from internodal myelin. In the course of this analysis, we unexpectedly discovered axonal changes associated with myelin outfoldings, which we further characterized. Together these data imply that diameters and shape of myelinated axons are sculpted by their myelin sheaths, a function that requires structural myelin proteins including PLP or MAG.

2 | RESULTS

To approach the three-dimensional morphology of pathological myelin outfoldings, we performed focused ion beam-scanning electron microscopy (FIB-SEM) of optic nerves dissected from *Plp*$^{-/Y}$ and *Mag*$^{-/-}$ mutant mice. Both models were previously shown to display myelin outfoldings according to the quantitative scrutiny of conventional two-dimensional transmission electron micrographs (TEM) (Patzig, Erwig, et al., 2016). For sample preparation, optic nerves of male adult (P75) mice were fixed and processed essentially following the osmium tetroxide—thiocarbohydrazide—osmium (OTO) method (Deerinck et al., 2010), which was recently shown to enable appropriate contrast to assess axon/glia-units (Weil et al., 2018) and myelin (Steyer et al., 2020). In each tissue block, >1000 FIB-SEM sections were scanned with a voxel size of 5 nm × 5 nm × 25 nm, thereby covering a volume of ≥15 μm × ≥ 15 μm × ≥ 25 μm. Assessing these datasets, we reconstructed all myelin outfoldings (highlighted in yellow) and their underlying axonal segment (highlighted in blue) in three dimensions in each of the tissue volumes obtained from control mice (Video 1, Figure 1a, a′ and Supplementary Figure 1), *Plp*$^{-/Y}$ mice (Video 2, Figure 1b, b′ and Supplementary Figure 2) and *Mag*$^{-/-}$ mice (Video 3, Figure 1c, c′ and Supplementary Figure 3). As expected from the previous quantitative assessment of two-dimensional TEM micrographs (Patzig, Erwig, et al., 2016), all mutant mice displayed a considerable number of myelin outfoldings per tissue volume (Videos 1–3; supplementary Figures 1–3). Control nerves also displayed some myelin outfoldings, though their number was markedly smaller compared to that in mutant mice. Importantly, none of the myelin outfoldings observed three-dimensionally had the needle-like shape that appears on two-dimensional electron micrographs (Patzig,

10981136, 2023, 3, Downloaded from https://onlinelibrary.wiley.com/doi/10.1002/glia.24290 by University Of Glasgow, Wiley Online Library on [24/01/2023]. See the Terms and Conditions (https://onlinelibrary.wiley.com/terms-and-conditions) on Wiley Online Library for rules of use; OA articles are governed by the applicable Creative Commons License

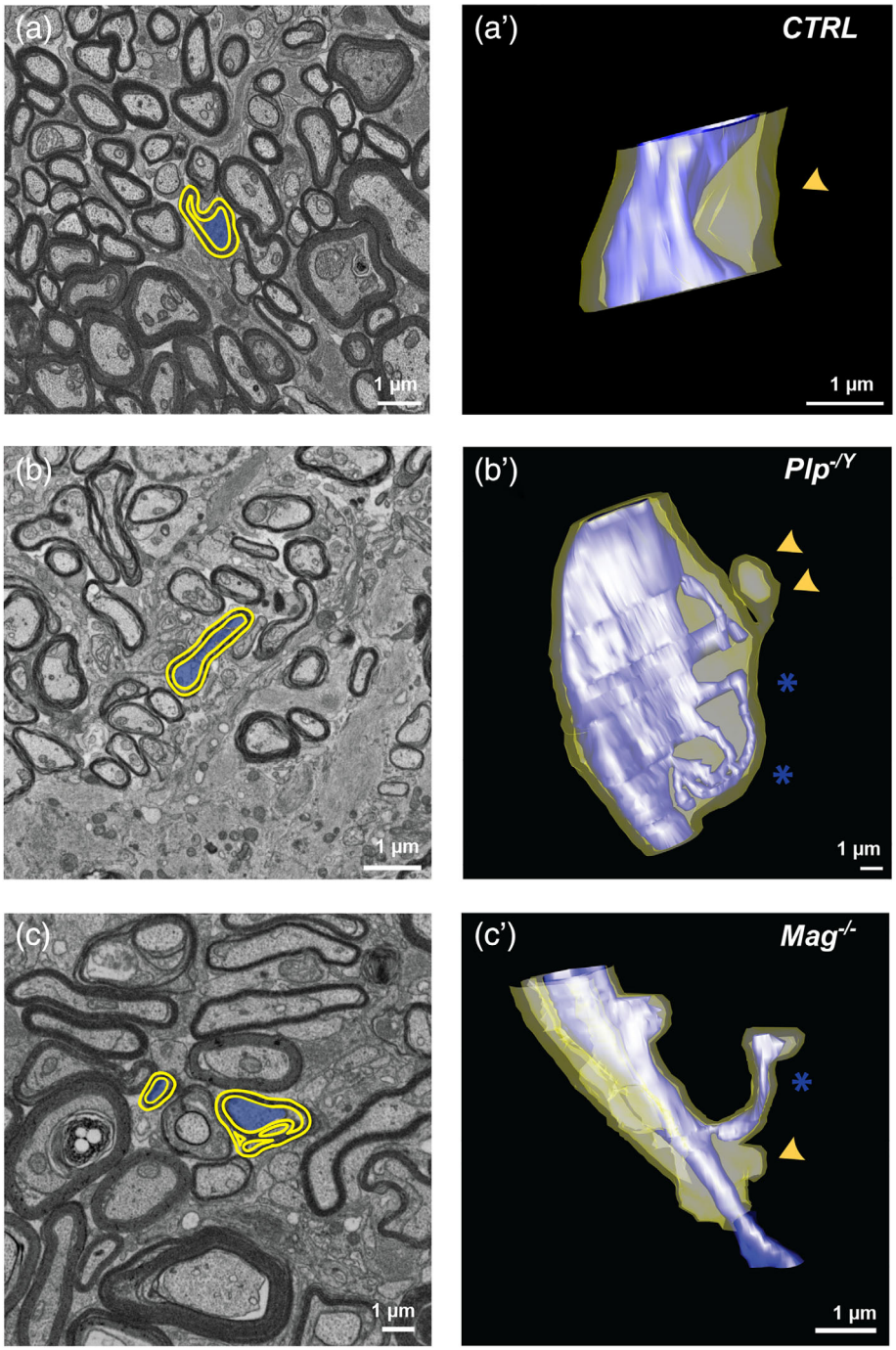

FIGURE 1 Three-dimensional reconstruction of myelin outfoldings. Focused ion beam-scanning electron microscopy (FIB-SEM) micrographs (a–c) and three-dimensional (3D) reconstruction (a′–c′) of representative myelin outfoldings (yellow) and the respective axonal segment (blue) in the optic nerve of myelin mutant and control mice. In each tissue block, >1000 FIB-SEM sections were scanned to cover a volume of ≥15 µm × ≥ 15 µm × ≥ 25 µm with a voxel size of 5 nm × 5 nm × 25 nm. Control (CTRL) (a, a′), *Plp*$^{-/Y}$ (b, b′), and *Mag*$^{-/-}$ (c, c′) mice were analyzed at postnatal day (P75). Myelin outfoldings reconstructed in (a′–c′) are also highlighted on the FIB-SEM micrographs in (A–C). Yellow arrowheads point at myelin outfoldings (a′–c′); blue stars mark an anastomosed axon (B′) and an axonal sprout (c′). Three mice per genotype and one tissue block per mouse were analyzed; one representative myelin outfolding per genotype is highlighted. Scale bars, 1 µm. For reconstructions of all myelin outfoldings in the tissue blocks, see supplemental Figure 1–3 and Videos 1–3. For genotype-dependent quantifications, see Figure 2.

Erwig, et al., 2016). Rather they are sheets of multilayered membrane, which extend along and away from the underlying myelinated axons.

When measuring the dimensions of myelin outfoldings, we found lengths along the axon of up to 10 µm as well as volumes of up to 38 µm^3 in mutant optic nerves, compared to up to 6 µm length along the axon and up to 10 µm^3 volume in controls (Figure 2a, b). Notably, myelin outfoldings displayed a range of dimensions. Indeed, only the larger outfoldings among those observed in mutant nerves exceeded the size of those in control nerves. Together, when using FIB-SEM to compare myelin outfoldings in the optic nerves of control mice with those in myelin mutants, the latter display more outfoldings, with some among them markedly larger in size.

We next assessed our FIB-SEM datasets to determine from which myelin segment pathological myelin outfoldings emerge. For this measurement, the internodal segment was defined as ≥2.5 µm away from the nearest node of Ranvier. We found that most of the assessed myelin outfoldings were associated with the internodal segment in *Mag*$^{-/-}$ and control mice (Figure 2c). In *Plp*$^{-/Y}$ mice about half of the

10981136, 2023, 3, Downloaded from https://onlinelibrary.wiley.com/doi/10.1002/glia.24290 by University Of Glasgow, Wiley Online Library on [24/01/2023]. See the Terms and Conditions (https://onlinelibrary.wiley.com/terms-and-conditions) on Wiley Online Library for rules of use; OA articles are governed by the applicable Creative Commons License

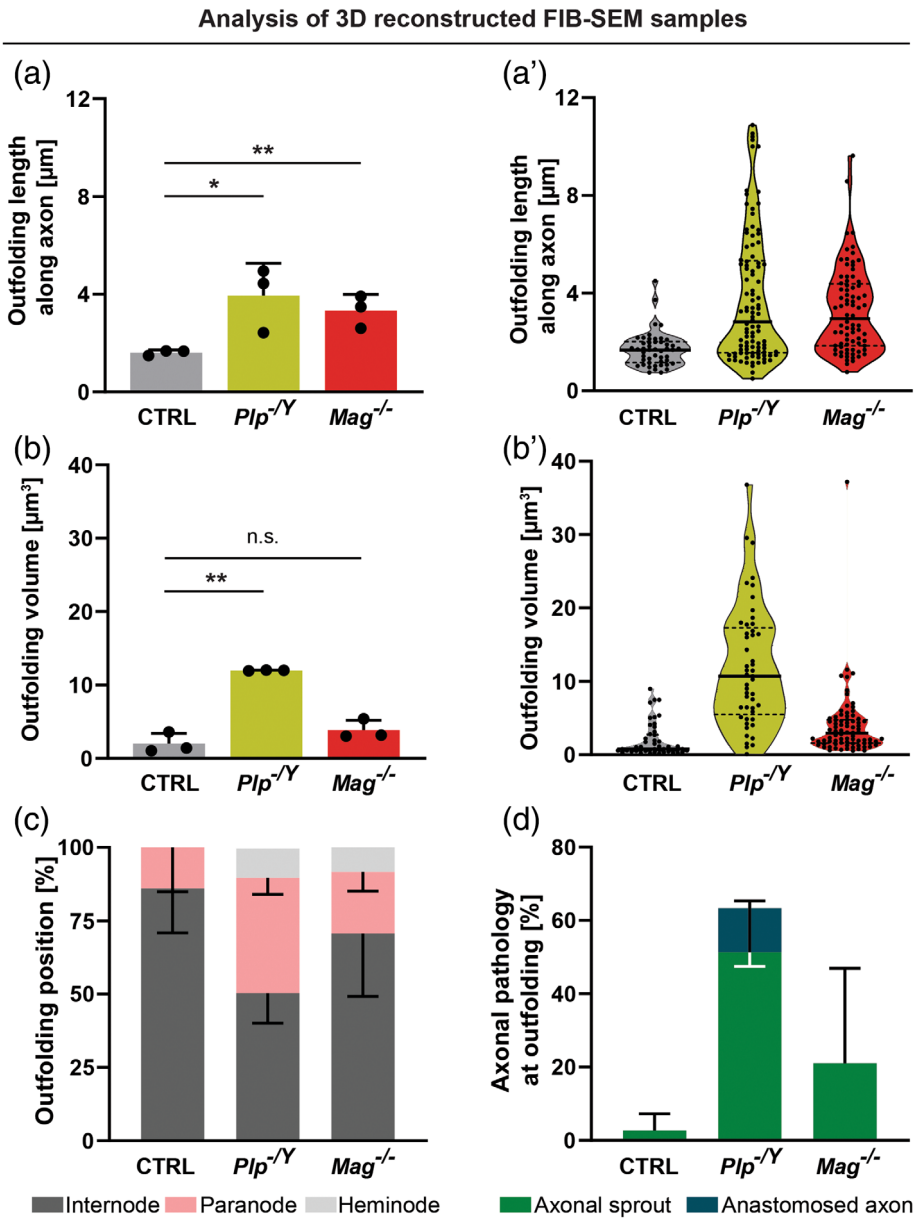

FIGURE 2 Genotype-dependent quantification of features of myelin outfoldings upon 3D-reconstruction of FIB-SEM micrographs. (a, a′) bar graph (a) and violin plot (a') showing the longitudinal extent along the axon of myelin outfoldings displayed in Figure 1, supplemental Figures 1–3, and Videos 1–3. Three mice per genotype and one tissue block per mouse were analyzed. Only outfoldings entirely comprised in the scanned tissue volume were included. (a) Mean ± SEM; data points represent individual mice. One-tailed t-test CTRL versus *Plp*$^{-/Y}$ $p = .0466$*, CTRL versus *Mag*$^{-/-}$ $p = .0057$**. (a′) Median with interquartile ranges; data points represent individual myelin outfoldings in the analyzed tissue volumes of three mice. (b, b′) Bar graph (b) and violin plot (b') showing the volume of the assessed myelin outfoldings. Three mice per genotype and one tissue block per mouse were analyzed. Only outfoldings entirely comprised in the scanned tissue volume were included. (b) Mean +/ SEM, data points represent individual mice. One-tailed t-test CTRL versus *Plp*$^{-/Y}$ $p = .0031$**, CTRL versus *Mag*$^{-/-}$ $p = 0.0849$ n.s. (b′) Median with interquartile ranges; data points represent individual myelin outfoldings. (c) Position of myelin outfoldings in the assessed tissue volumes relative to the axonal segment (internodal, paranodal, and heminodal). The internodal segment was defined as a distance of ≥2.5 µm away from a node of Ranvier. Note that the majority of myelin outfoldings emerges from the internode. Mean /− SEM. (d) Pathological features of axons underneath myelin outfoldings. Mean ± SEM.

outfoldings were found at the paranodes/heminodes (Figure 2c). In both *Plp*$^{-/Y}$ and *Mag*$^{-/-}$ mice, a number of myelin outfoldings was also found at heminodes (Figure 2c), i.e., at paranodes lacking a neighboring myelin sheath, probably reflecting that these mice display hypomyelination.

When assessing the morphology of axons underneath myelin outfoldings upon three-dimensional reconstruction of FIB-SEM datasets, we observed an unexpectedly frequent occurrence of axonal pathology, which we quantified. Indeed, a considerable number of axons underneath myelin outfoldings in *Plp*$^{-/Y}$ and *Mag*$^{-/-}$ mice

10981136, 2023, 3, Downloaded from https://onlinelibrary.wiley.com/doi/10.1002/glia.24290 by University Of Glasgow, Wiley Online Library on [24/01/2023]. See the Terms and Conditions (https://onlinelibrary.wiley.com/terms-and-conditions) on Wiley Online Library for rules of use; OA articles are governed by the applicable Creative Commons License

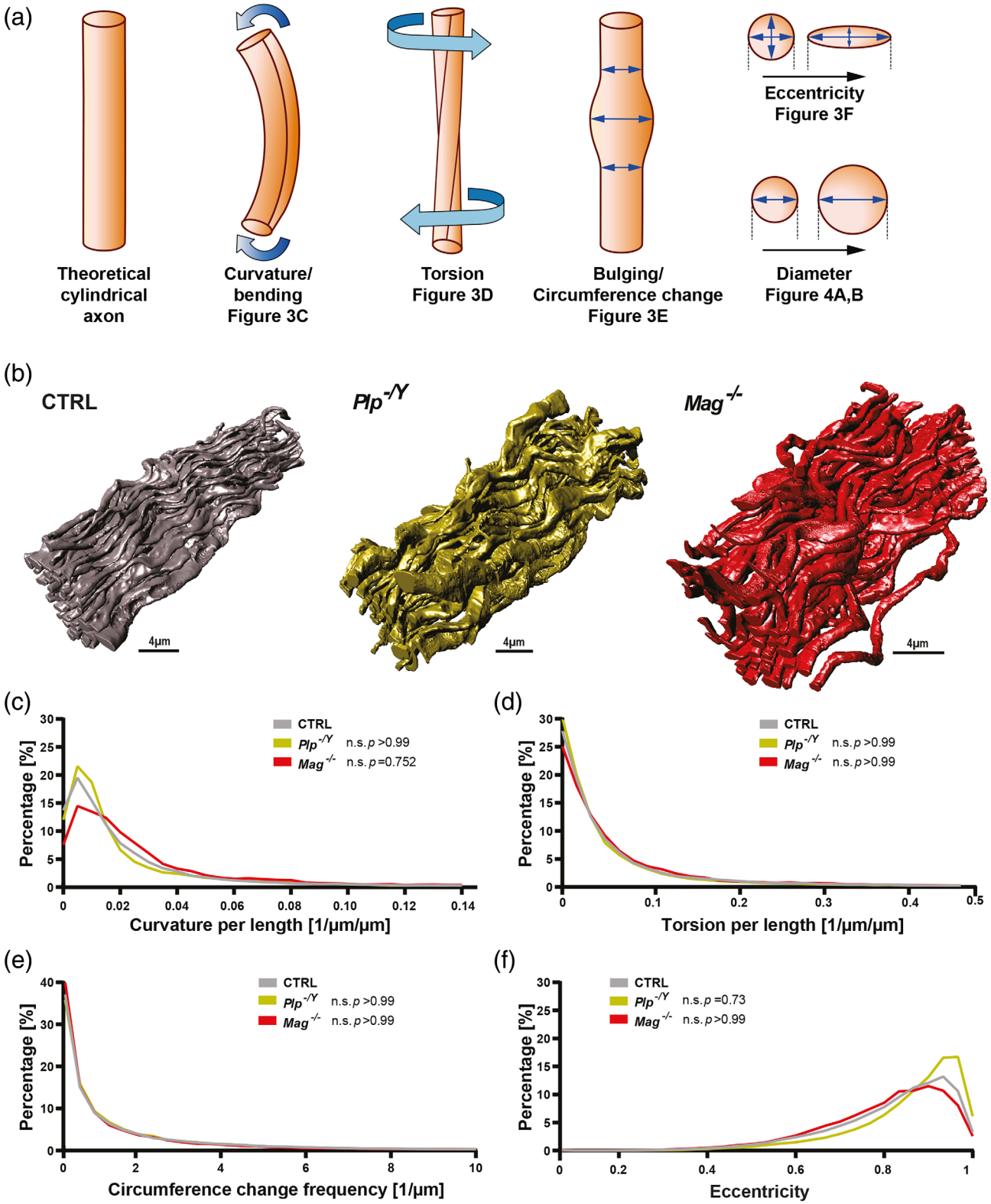

FIGURE 3 Genotype-dependent assessment of axonal shape upon 3D-reconstruction of FIB-SEM micrographs. (a) Scheme illustrating quantified axonal features diverging from a theoretical cylindrical shape. For analysis groups also see Supplemental Figure 4. (b) 3D-reconstructed FIB-SEM tissue volumes of optic nerves dissected from *Plp*$^{-/Y}$, *Mag*$^{-/-}$, and control (CTRL) mice. A total of 50 axonal segments were reconstructed and assessed in FIB-SEM volumes of one mouse per genotype. Scale bar lengths are indicated. (c) Frequency distribution of axonal curvature per 1 µm axonal length calculated from the data in Figure 3b. n.s., not significant. (d) Frequency distribution of axonal torsion per 1 µm axonal length calculated from the data in Figure 3b. n.s., not significant. (e) Frequency distribution of axonal bulging calculated as the change of circumference per 1 µm axonal length from the data in Figure 3b. n.s., not significant. (f) Frequency distribution of axonal eccentricity per 1 µm axonal length calculated from the data in Figure 3b. n.s., not significant.

10981136, 2023, 3, Downloaded from https://onlinelibrary.wiley.com/doi/10.1002/glia.24290 by University Of Glasgow, Wiley Online Library on [24/01/2023]. See the Terms and Conditions (https://onlinelibrary.wiley.com/terms-and-conditions) on Wiley Online Library for rules of use; OA articles are governed by the applicable Creative Commons License

displayed collateral outgrowths that terminated underneath the myelin sheath, i.e., axonal sprouts (Figure 1c′ and Figure 2d). Additionally, axons diverging into branches and reuniting, i.e., anastomosed axons, were observed underneath myelin outfoldings in *Plp*$^{-/Y}$ mice (Figure 1b′ and Figure 2d). To the best of our knowledge, these pathological features were not previously reported. Taken together, both models display myelin outfoldings associated with axonal sprouts; however, they show differences with respect to the frequencies of affected axonal segments and underlying axonal pathology.

These unexpected observations, and considering the recent finding that axonal shape and diameter depend on the axon's microenvironment (Andersson et al., 2021; Giacci et al., 2018), motivated us to assess the shape and diameter of myelinated optic nerve axons in these myelin mutants more systematically, i.e., irrespective of the local occurrence of myelin outfoldings or axonal pathology (see scheme in Figure 3a). We thus reconstructed the shapes of 50 axons per tissue volume in *Plp*$^{-/Y}$ and *Mag*$^{-/-}$ mice (Figure 3b). From these data, it was possible to calculate longitudinal axonal curvature (Figure 3c), torsion (Figure 3d), bulging (i.e., change of circumference along the axon) (Figure 3e), and eccentricity (Figure 3f) over a length of ≥20 μm. However, none of these parameters differed significantly in the assessed myelin mutants compared to controls (Figure 3c–f).

To quantify the diameters of myelinated axons, we turned to two-dimensional TEM, which allows measuring a markedly larger number of axons compared to FIB-SEM. We found that the diameters of myelinated axons were considerably enlarged in *Plp*$^{-/Y}$ and *Mag*$^{-/-}$ mice compared to respective controls (Figure 4a, b). Thus, both models displayed increased diameters of myelinated axons without affecting other principal parameters of axonal shape.

Aiming to enable comparisons with prior reports, we finally assessed various other pathological features in *Plp*$^{-/Y}$ and *Mag*$^{-/-}$ mice at P75 on two-dimensional TEM micrographs of optic nerves. Indeed, *Mag*$^{-/-}$ mice displayed reduced axonal density while *Plp*$^{-/Y}$ mice showed a trend toward reduced axonal density that did not reach significance (Figure 4c). Both models showed a reduced percentage of myelinated axons (Figure 4d) and an increased percentage of axon/myelin-units with myelin outfoldings (Figure 4e). Axonal swellings were a feature in *Plp*$^{-/Y}$ but not *Mag*$^{-/-}$ mice (Figure 4f). Other, less frequent pathological features of the axon/myelin-unit including double myelination, myelinoid bodies and inner tongue swellings were significantly increased in *Plp*$^{-/Y}$ mice and showed a trend toward increased occurrence that did not reach significance in *Mag*$^{-/-}$ mice (Figure 4g). As far as these features were previously reported, to the best of our knowledge our present assessment in Figure 4c–g is in agreement with prior results (Table 1).

In summary, we find that the mouse models lacking the structural myelin proteins PLP or MAG display myelin outfoldings associated with underlying axonal sprouting or anastomosing, and that the diameters of myelinated axons in both models are increased. This implies that structural myelin integrity is a relevant factor in restricting radial axonal expansion.

3 | DISCUSSION

Myelin outfoldings are a frequent pathology in the CNS, but their shape and origin has remained poorly characterized. One reason is probably that the commonly used two-dimensional TEM provides only limited information about three-dimensional features. For example, two-dimensional TEM visualizes the most CNS myelin outfoldings with a needle-like shape pointing away from the underlying myelinated axon. Here we scrutinized myelin outfoldings in the optic nerves of *Plp*$^{-/Y}$ and *Mag*$^{-/-}$ mutant mice using FIB-SEM, which enables three-dimensional reconstruction of axon/myelin units in a volume of CNS tissue. We find that CNS myelin outfoldings do not display needle-like shape; instead, they are large sheets with a longitudinal dimension along the axon of up to 10 μm. More than half of all assessed CNS myelin outfoldings emerged from internodal segments. We speculate that the myelin outfoldings in these models reflect a generally reduced stability of their myelin compared to healthy sheaths.

Outfoldings of myelin sheaths are also a frequent pathological feature in disorders of the peripheral nervous system (PNS) (neuropathies) and the respective rodent models (Adlkofer et al., 1995; Goebbels et al., 2012; Golan et al., 2013; Horn et al., 2012; Hu et al., 2016; Kammers et al., 2015; Kim et al., 2016; Yin et al., 1998). Also referred to as tomaculae, focal hypermyelination, or redundant myelin, peripheral myelin outfoldings emerge from the noncompact subcompartments of myelin, i.e. paranodes and Schmidt-Lanterman incisures, which are considered sites of local instability when compared to the otherwise compacted myelin sheath. We thus speculate that the presence of myelin outfoldings in the CNS reflects reduced myelin stability along the entire internode, rather than locally at sites of noncompact myelin as in the PNS. With respect to axonal enlargement as observed in both models, we cannot formally exclude yet-unidentified underlying changes in myelin-to-axon signaling. However, we consider it more plausible that impaired myelin stability per se provides less resistance against intrinsic radial expansion of axons and thus enables increased axonal diameters. One may conceive that enlargement of axons leads to increased stiffness, thereby stabilizing against bending. However, we did not observe altered axonal shapes, such as curvature, torsion, bulging, or eccentricity. Most likely, in addition to the myelin sheath, the axonal plasma membrane and cytoskeleton, including neurofilaments and the actin/myosin/spectrin-network (Costa et al., 2018, 2020), provide physical stability against abnormal axonal shape. For example, axonal diameters are increased in mice lacking α-adducin, a regulator of actin/spectrin-ring assembly (Leite et al., 2016).

Additional to abnormal radial axonal growth, preferential loss, due to degeneration, of smaller diameter axons may contribute to the frequency distribution shift toward larger axonal diameters. Indeed, for *Plp*-mutant mice it has been previously suggested that small diameter axons are more susceptible to degeneration because the optic nerve and fasciculus gracilis, which comprise small-diameter axons, display axonal swellings before fiber tracts comprising larger-diameter axons are also affected (Edgar et al., 2004; Garbern et al., 2002).

10981136, 2023, 3, Downloaded from https://onlinelibrary.wiley.com/doi/10.1002/glia.24290 by University Of Glasgow, Wiley Online Library on [24/01/2023]. See the Terms and Conditions (https://onlinelibrary.wiley.com/terms-and-conditions) on Wiley Online Library for rules of use; OA articles are governed by the applicable Creative Commons License

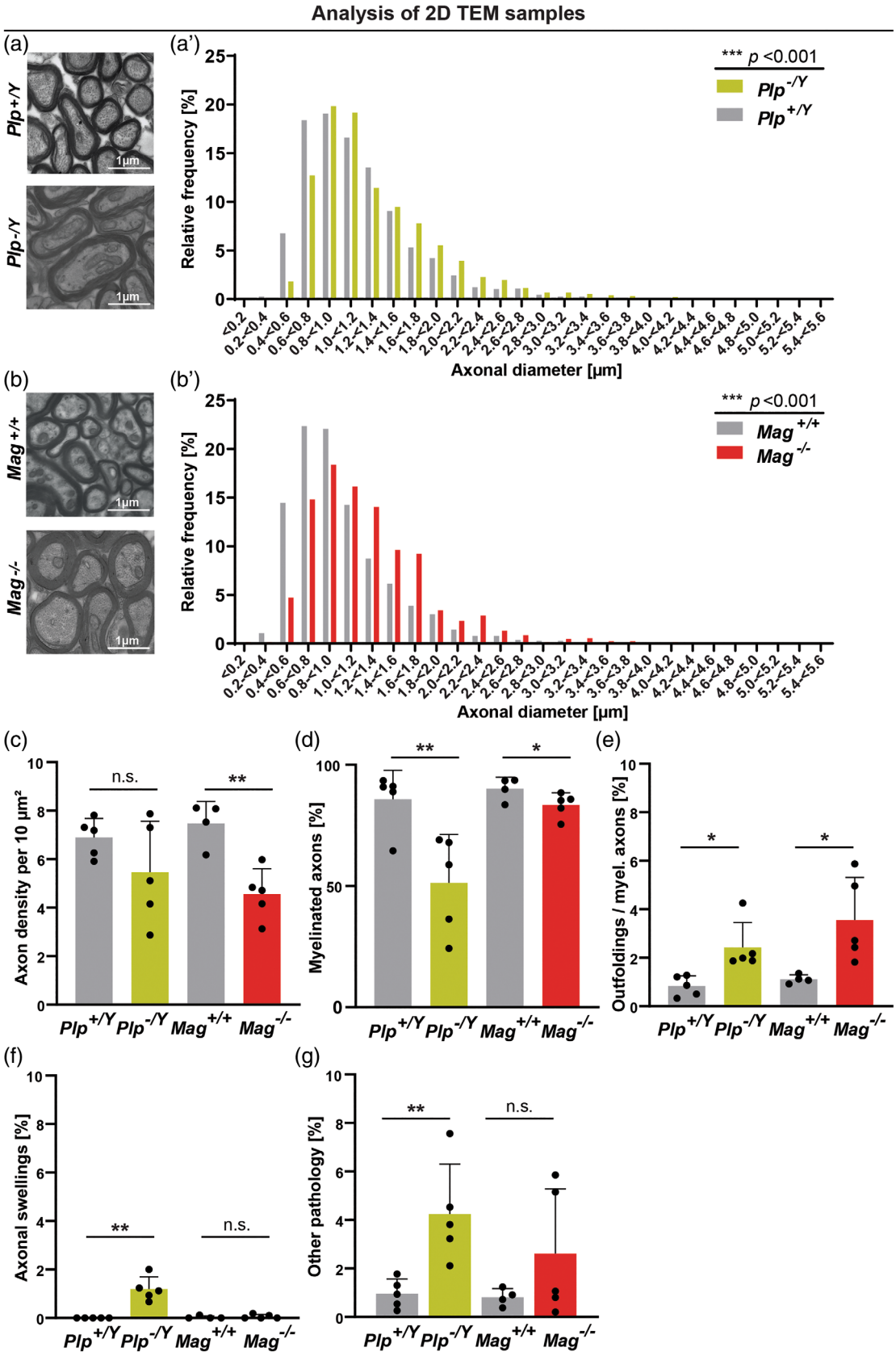

FIGURE 4 Legend on next page.

10981136, 2023, 3, Downloaded from https://onlinelibrary.wiley.com/doi/10.1002/glia.24290 by University Of Glasgow, Wiley Online Library on [24/01/2023]. See the Terms and Conditions (https://onlinelibrary.wiley.com/terms-and-conditions) on Wiley Online Library for rules of use; OA articles are governed by the applicable Creative Commons License

TABLE 1 Comparison of neuropathological features in the CNS of *Plp*$^{-/Y}$ and *Mag*$^{-/-}$ mice

Feature	Proteolipid protein (PLP)	Myelin-associated glycoprotein (MAG)
Topology	Cholesterol-associated tetra-span	Ig-like type I single-span
% of total CNS myelin protein	38% (Jahn et al., 2020)	0.7% (Jahn et al., 2020)
Associated human spastic paraplegia (SPG) type	SPG2 (Saugier-Veber et al., 1994; Garbern et al., 2002; Inoue, 2019; Cailloux et al., 2000)	SPG75 (Novarino et al., 2014; Lossos et al., 2015; Roubertie et al., 2019; Zech et al., 2020)
Pathological feature		
Mouse model	*Plp*$^{-/Y}$ mice	*Mag*$^{-/-}$ mice
First publication	(Klugmann et al., 1997)	(C. Li et al., 1994; Montag et al., 1994)
Reduced percentage of axons myelinated (hypomyelination)	(De Monasterio-Schrader et al., 2013; Patzig, Erwig, et al., 2016; Yool et al., 2001); this study	(C. Li et al., 1998; Bartsch et al., 1997; Biffiger et al., 2000; Patzig, Erwig, et al., 2016; Pernet et al. 2008); this study
Myelin outfoldings (focal hypermyelination)	(Patzig, Erwig, et al., 2016); this study	(C. Li et al., 1994; C. Li et al., 1998; Biffiger et al., 2000; Patzig, Erwig, et al., 2016); this study
Axonal swellings	(Edgar et al., 2004; Griffiths et al., 1998; Steyer et al., 2020) this study	n.a.
Axon loss	n.a.	(Nguyen et al., 2009); this work
Increased diameter of myelinated axons	(Yool et al., 2001); this study[a]	This study[a]
Axonal sprouting	This study[b]	This study[b,c]
Axonal anastomoses	This study[b]	n.a.[b]

Note: Features of PLP and MAG, neuropathological features in *Plp*$^{-/Y}$ and *Mag*$^{-/-}$ mice, and key references are given. Data in the present study are based on assessment of optic nerves at age P75. Data from the previous studies are based on assessment of various CNS regions at various ages (see respective studies).
Abbreviation: SPG, spastic paraplegia.
[a]Of normal-appearing axon/myelin-units.
[b]Underneath myelin outfoldings.
[c]Axonal sprouting was previously reported in *Mag*$^{-/-}$ mutants upon challenge by injury.

Yet, considering that the optic nerves of *Plp*-mutant mice at P75 display a highly significant shift in frequency distribution toward larger axonal diameters but only a slight trend toward reduced axonal density, selective loss of smaller diameter axons is unlikely the definitive explanation for the observed frequency shift. *Mag*-mutants display degenerating CNS axons (Nguyen et al., 2009; Pan et al., 2005) and a reduced total number of axons (Nguyen et al., 2009) in the spinal cord dorsal column; however, these analyses specifically focused on this

FIGURE 4 Genotype-dependent assessment of two-dimensional transmission electron micrographs reveals that diameters of myelinated axons are increased in the optic nerves of *Plp*$^{-/Y}$ and *Mag*$^{-/-}$ mice. (a, a', b, b′) Conventional two-dimensional transmission electron micrographs of cross-sectioned optic nerves (a, b) and genotype-dependent quantification (a', b') reveals increased axonal diameters in *Plp*$^{-/Y}$ (a, a') and *Mag*$^{-/-}$ (b, b') compared to respective littermate control mice at P75. (a, b) Example images; Scale bars 1 μm. (a', b') > 150 axons per mouse were assessed on ≥10 randomly distributed electron micrographs per mouse in 5 mice per genotype. Data presented as frequency distribution with 0.2 μm bin width. Two-sided Kolmogorov–Smirnov test of frequency distribution reveals shift to increased diameters of axons; *Plp*$^{+/Y}$ versus *Plp*$^{-/Y}$ $p = 7.1 \times 10–9$*** (a'), *Mag*$^{+/+}$ vs *Mag*$^{-/-}$ $p = 2.2 \times 10^{-16}$*** (b'). (c–g) Quantitative assessment of morphological features of axon/myelin units on transmission electron micrographs of optic nerve sections of *Plp*$^{-/Y}$ and *Mag*$^{-/-}$ mice compared to respective control littermates at P75. >550 axons per mouse were assessed on ≥10 randomly distributed electron micrographs per mouse in 4–5 mice per group. Data represent mean ± SEM; datapoints represent individual mice. (c) Quantitative assessment of axonal density. Data represent mean axon number in 10 μm rectangles. One-tailed *t*-test CTRL versus *Plp*$^{-/Y}$ $p = .1057$ n.s., CTRL vs *Mag*$^{-/-}$ $p = .0015$**. (d) Quantitative assessment of the percentage of axons that is myelinated. One-tailed t-test CTRL versus *Plp*$^{-/Y}$ $p = .0072$**, CTRL versus *Mag*$^{-/-}$ $p = .04$*. (e) Quantitative assessment of the percentage of myelinated axons that display myelin outfoldings. One-tailed *t*-test CTRL versus *Plp*$^{-/Y}$ $p = .0107$*, CTRL versus *Mag*$^{-/-}$ $p = .0176$*. (f) Quantitative assessment of the percentage of axon/myelin units that display axonal swellings. One-tailed *t*-test CTRL vs *Plp*$^{-/Y}$ $p = .0029$**, CTRL versus *Mag*$^{-/-}$ $p = .2914$ n.s. (g) Quantitative assessment of the percentage of axon/myelin units that display other pathology including tubovesicular structures and amorphous axoplasm in an axon, inner tongue swellings, myelinoid bodies, absence of an identifiable axon in a myelin sheath and myelin whorls. One-tailed *t*-test CTRL versus *Plp*$^{-/Y}$ $p = .0012$**, CTRL versus *Mag*$^{-/-}$ $p = .1087$ n.s.

10981136, 2023, 3, Downloaded from https://onlinelibrary.wiley.com/doi/10.1002/glia.24290 by University Of Glasgow, Wiley Online Library on [24/01/2023]. See the Terms and Conditions (https://onlinelibrary.wiley.com/terms-and-conditions) on Wiley Online Library for rules of use; OA articles are governed by the applicable Creative Commons License

fiber tract and thus do not allow comparison with other tracts with larger diameter fibers. Together, increased radial axonal growth and preferential loss of smaller diameter axons may both contribute to the frequency distribution shift toward larger axonal diameters in the CNS of both mutant models, though the latter not to axonal sprouting and anastomosing.

PLP, the most abundant CNS myelin protein and an adhesive force within compact myelin (Bakhti et al., 2013; Bizzozero et al., 2001; Sinoway et al., 1994), facilitates myelin compaction at the extracellular intraperiod lines and thus stability along the entire sheath (Boison et al., 1995; Klugmann et al., 1997; Möbius et al., 2008). It is thus plausible that, when PLP is lacking, reduced myelin stability does not only allow surplus radial growth of axons but also permits axonal sprouting and the formation of anastomoses. It is unclear whether the axonal sprouts and anastomoses seen in *Plp*$^{-/Y}$ mice represent an early stage of axonopathy that later develops into the previously observed axonal swellings (Griffiths et al., 1998; Lüders et al., 2017, 2019; Patzig, Kusch, et al., 2016; Steyer et al., 2020; Trevisiol et al., 2020) or if they represent a separate neuropathological feature.

The adhesion between compact myelin layers is not impaired in mice lacking MAG. However, MAG is an Ig-CAM expressed at the adaxonal myelin surface (Erb et al., 2006; Trapp & Quarles, 1984) with functions in both axomyelinic adhesion (Djannatian et al., 2019; Elazar et al., 2019; Kinter et al., 2013; Li et al., 1994; Montag et al., 1994) and inhibitory signaling, at least upon injury (Liu et al., 2002; McKerracher et al., 1994; Mukhopadhyay et al., 1994). Indeed, MAG inhibits axonal sprouting *in vitro* as well as *in vivo* upon spinal cord injury (Lee et al., 2010; Li et al., 2004; Shen et al., 1998; Sicotte et al., 2003). Thus, our observations demonstrate that the inhibitory function of MAG in the CNS is not limited to injury conditions but also involved in regulating radial axonal growth and axonal sprouting in the non-injured CNS.

Thus, despite some apparent similarities in the CNS pathology that emerges when mice lack PLP or MAG, the proteins differ regarding their respective localization in compact versus adaxonal myelin, and in their functions as structural tetraspan-protein versus repulsive Ig-CAM. Strikingly, the axonopathy also differs principally between the models. Indeed, when PLP is lacking axons display characteristic axonal swellings but comparatively slowly progressive axon loss. Conversely, when MAG is lacking, axons degenerate without the formation of axonal swellings. Thus, not only different frequencies of the same pathological feature but also principal differences exist between the models, highlighting that the functional relevance of these myelin proteins remain to be further investigated.

It is noteworthy that the diameters of myelinated axons are reduced in the PNS of *Mag*$^{-/-}$ mutant mice (Eichel et al., 2020; Pan et al., 2005; Yin et al., 1998). How can deficiency of the same myelin protein have opposite effects on axonal diameters in the CNS and the PNS? Notably, the protein composition of CNS and PNS myelin differ considerably (Jahn et al., 2020; Siems et al., 2020), thus providing a markedly different molecular microenvironment to the myelinated axon. For example, the adaxonal surface of PNS myelin—but not of CNS myelin—exposes chemokine-like factor-like MARVEL-transmembrane domain-containing protein 6 (CMTM6) to the myelinated axon (Eichel et al., 2020). Deletion of *Cmtm6*-expression in Schwann cells causes increased diameters of peripheral axons, and, importantly, deleting *Cmtm6* from Schwann cells in addition to *Mag*-deficiency actually also leads to enlarged axonal diameters. The fact that PNS myelin—but not CNS myelin—comprises CMTM6 additional to MAG may thus explain the oppositely-shifted axonal diameters in the PNS and CNS of *Mag*-single mutant mice. However, additional, not yet identified factors are likely to contribute to determining axonal diameters.

In both models assessed here, the presence of myelin outfoldings also coincides with a diminished abundance of myelin septins, which form a stabilizing filament in the adaxonal myelin compartment (Patzig, Erwig, et al., 2016). Myelin outfoldings are also observed in the developing CNS. For example, many axon/myelin-units in the optic nerve of Xenopus tadpoles display myelin outfoldings, which are largely resolved upon metamorphosis (Cullen & Webster, 1979). Indeed, during developmental myelination the initial wrapping phase is followed by a maturation phase in which surplus myelin sheaths and myelin outfoldings are remodeled (Rosenbluth, 1966). The developmental elimination of myelin outfoldings is not limited to metamorphosing amphibia, as shown by two-dimensional TEM of the optic nerves of mice (Djannatian et al., 2021; Patzig, Erwig, et al., 2016; Snaidero et al., 2014). Here, the proportion of axon/myelin-units that displays myelin outfoldings declines considerably between the second postnatal week and an age of 2–3 months. The developmental elimination of myelin outfoldings coincides with the emergence of the stabilizing septin filament in adaxonal myelin (Patzig, Erwig, et al., 2016). It will be an interesting future experiment to assess if the developmental elimination of myelin outfoldings per se also counteracts axonal sprouting or anastomosing.

We cannot formally exclude that increased axonal diameters, sprouting and anastomoses as observed here represent active axonal expansion. If so, this would probably involve the activation or impairment of yet-unknown myelin-to-axon signaling mechanisms. However, we consider it more likely that the loss of structural myelin proteins including PLP and MAG causes reduced stability of the myelin sheath, thereby rendering it less suited to limit axon-intrinsic radial growth that may take place if not sufficiently counteracted. In conclusion, this work supports the concept that healthy myelin sheaths not only preserve the long-term integrity of their myelinated axons (Duncan et al., 2021; Nave & Werner, 2021; Philips & Rothstein, 2017) but also affect their diameter and shape. Axonal changes secondary to impaired physical myelin stability may emerge as a unifying feature in the pathogenesis of myelin mutants with secondary axonal pathology.

4 | MATERIALS AND METHODS

4.1 | Ethics

Animal welfare: For the procedure of sacrificing vertebrates for the subsequent preparation of tissue, all regulations given in the German animal welfare law (TierSchG §4) are followed. Since sacrificing of

10981136, 2023, 3, Downloaded from https://onlinelibrary.wiley.com/doi/10.1002/glia.24290 by University Of Glasgow, Wiley Online Library on [24/01/2023]. See the Terms and Conditions (https://onlinelibrary.wiley.com/terms-and-conditions) on Wiley Online Library for rules of use; OA articles are governed by the applicable Creative Commons License

vertebrates is not an experiment on animals according to §7 Abs. 2 Satz 3 TierSchG, no specific ethical review and approval or notification is required for the present work. All procedures were supervised by the animal welfare officer and the animal welfare committee for the Max Planck Institute of Multidisciplinary Sciences, Göttingen, Germany. The animal facility at the Max Planck Institute of Multidisciplinary Sciences is registered according to §11 Abs. 1 TierSchG.

4.2 | Sample preparation and transmission electron microscopy (TEM)

Mice harboring *null*-alleles of the *Plp/Plp1* and *Mag* genes were previously reported (Klugmann et al., 1997; Lappe-Siefke et al., 2003; Montag et al., 1994; Patzig, Erwig, et al., 2016) and maintained on a c57Bl/6 N background for at least 10 generations. $Plp^{-/Y}$ and $Mag^{-/-}$ mice and respective wild type littermates were sacrificed by cervical dislocation at postnatal day 75 (P75). The optic nerves were dissected and immersion fixed and prepared using the reduced osmium tetroxide—thiocarbohydrazide - osmium (OTO) method as the previously described in detail (Steyer et al., 2020; Weil et al., 2018) upon implementing modifications to the original protocol first introduced by (Deerinck et al., 2010). After resin polymerization, ultrathin sections (60–70 nm) were cut using an ultramicrotome (Leica UC-7, Vienna, Austria) and a 35° diamond knife (Diatome, Biel, Switzerland). The sections were placed on 100 mesh hexagonal copper grids (Science Services, Munich, Germany) and imaged with a Leo 912 electron microscope (Carl Zeiss, Oberkochen, Germany) and an on-axis 2 k CCD camera (TRS, Moorenweis, Germany).

4.3 | Axon diameter analysis on transmission electron micrographs

To determine axonal diameters, 10–15 random non-overlapping electron micrographs (13.43 μm^2 /image) per mouse and 4–5 mice per genotype were analyzed as specified in the figure legend. Analysis was performed using Fiji version 1.53c (Schindelin et al., 2012). Per electron micrograph, up to 30 axons were selected at random using the Grid-Tool (Circular grids, 3 μm^2 per point, random offset). The Feret diameter was analyzed of all normal appearing myelinated axons comprised in the grid circles. The Kolmogorov–Smirnov (KS) test was used to assess shifts in axonal diameters between experimental groups. For statistical analysis we used Rstudio (www.rstudio.com, version 3.4.1) as previously described in detail (Eichel et al., 2020) available at https://github.com/MariaEichel/FrequencyDistributions.

4.4 | Focused ion beam-scanning electron microscopy (FIB-SEM)

The samples were further trimmed with a 90° trimming diamond knife (Diatome) and multiple samples were placed on a SEM stub using silver conductive resin (EPO-TEK 129-4; Science Services, Munich, Germany) and sputter-coated using a high vacuum coater (ACE 600, Leica, Wetzlar, Germany) with 10 nm platinum or gold. Sputtered samples were placed in the FIB-SEM (Crossbeam 540, Zeiss, Oberkochen, Germany). A cross-section through the sample was exposed using 15/30 nA, followed by a polishing step of 7 nA. A deposition of 400–500 nm platinum was added on top of the target region using 3 nA. Datasets were acquired at 1.5 kV using the energy-selective backscatter detector (ESB) in analytical mode with a grid voltage of 450 V and a current of 1000 pA. Using a pixel size of 5 nm × 5 nm and a slicing thickness of 25 nm, volumes of ≥15 μm × ≥ 15 μm × ≥ 25 μm were acquired.

4.5 | Data processing and visualization

For the present work, the following steps were performed using Fiji (Schindelin et al., 2012). The datasets were aligned using the scale-invariant feature transform (SIFT) algorithm, cropped and inverted. The images were smoothed using a Gaussian blur (sigma 1) and a local contrast enhancement was applied (CLAHE: blocksize 127, histogram bins 256, maximum slope 1.5). Outfoldings were segmented on the unbinned data, while for the axonal analysis the datasets were binned by 6 in x/y. The carving workflow implemented in the software Ilastik (Sommer et al., 2011) was used to semi-automatically segment 50 axons per dataset for one littermate control and one mutant for each of the mouse lines. The final model was corrected manually using Microscopy Image Browser (Belevich et al., 2016) and exported as binary tiff images for further analysis. The FIB-SEM micrograph datasets of the $Plp^{-/Y}$ and the corresponding littermate control samples were previously used (Steyer et al., 2020; Trevisiol et al., 2020) as the basis to reconstruct and analyze features independent from those assessed in the present work.

4.6 | Data analysis

Image processing and analysis were performed using a self-written MATLAB code (The Mathworks, Inc., Natick, MA, USA). Images in tiff data format were saved as stacks of $x-y$ matrices. A logical mask was created, in which pixels belonging to the axons were set to 1 and all other pixels were set to 0. Connected areas of pixels with less than 50 pixels were categorized as noise and set to 0 as well. To ensure that separate axons were not connected merely by single pixels, axon signals in each $x-y$ matrix were eroded, employing a disk-shaped structuring element with a diameter of 7 pixels. Single, separate, three-dimensional axons were detected, and cubic pixel volumes were defined as connected if either their faces, edges or corners were in contact with each other; if indicated, some manual corrections were applied. Axons were manually categorized into three groups (see scheme in Supplemental Figure 4): group 1 contained axons where the central line can be described as a unique function of z and do not bend back (Supplemental Figure 4a), group 2 contained axons where the central line cannot be described as a unique function in

10981136, 2023, 3, Downloaded from https://onlinelibrary.wiley.com/doi/10.1002/glia.24290 by University Of Glasgow, Wiley Online Library on [24/01/2023]. See the Terms and Conditions (https://onlinelibrary.wiley.com/terms-and-conditions) on Wiley Online Library for rules of use; OA articles are governed by the applicable Creative Commons License

z (Supplemental Figure 4b), and group 3 contained axons with several separate areas per $x-y$ plane (Supplemental Figure 4c).

In group 1, an $x-y$ plane was defined for each z (Supplemental Figure 4a). The axon signal in the $x-y$ plane was shrank to a single, central point (x, y) using the MATLAB function "bwmorph(image, "shrink," Inf)," and the sequence of (x, y) coordinates was used to define the central line of the axon. In case our MATLAB code was unable to find a single point because there was a pixel-sized hole inside the axon, the average of both points found by the MATLAB function was saved as part of the central line of the axon. In group 2, the analysis of the axon was the same as in group 1 with the exception of the data that bent back in z. That section of the axon was manually selected and axon slices in the x-z or $y-z$ plane with a constant y or x value, respectively, were shrank to one point as above. The x, y and z coordinates of the central lines were smoothed. The smoothed coordinates in pixels were converted to nm with the pixel-to-nm ratio known from the FIB-SEM experiments. The contour length of the entire axon was calculated by summing up the Euclidian distances between the smoothed coordinates of one axon. The x, y and z coordinates of the central lines were smoothed again with respect to the contour length. In both groups, anastomoses or bulges may occur, so that several separate areas in one $x-y$ plane of one axon are detected, as schematically shown in Supplemental Figure 4c. In these cases, only the not-anastomosed axon, that is, the larger one, was analyzed. In case bulging caused more than one area per $x-y$ plane, the area connected to the axon and not to the bulge was analyzed.

The Frenet-Serret formulas define the relation between the curvature κ and torsion τ of the central line of an axon. Here, s is the arclength, $\boldsymbol{T}$ the tangential vector, $\boldsymbol{N}$ the normal vector and $\boldsymbol{B}$ the binormal vector (Sternberg, 2012):

$$\begin{aligned} \frac{d\boldsymbol{T}}{ds} &= \kappa \boldsymbol{N}, \\ \frac{d\boldsymbol{N}}{ds} &= -\kappa \boldsymbol{T} + \tau \boldsymbol{B}, \\ \frac{d\boldsymbol{B}}{ds} &= -\tau \boldsymbol{N}. \end{aligned} \tag{1}$$

where $\boldsymbol{N}$ is a unit vector and the derivative of the tangent, so that the curvature κ is calculated as follows:

$$\boldsymbol{N} = \frac{\frac{d\boldsymbol{T}}{ds}}{\left\|\frac{d\boldsymbol{T}}{ds}\right\|}, \kappa = \left\|\frac{d\boldsymbol{T}}{ds}\right\|.$$

The tangent vector was smoothed. From the normal vector, the binormal vector was calculated using Equation (1) and smoothed again. The torsion was calculated from the single components i of the normal and binormal vector:

$$\frac{dB_i}{ds} = -\tau N_i \Rightarrow \tau = -\frac{\frac{dB_i}{ds}}{N_i}.$$

In case of numeric deviations between the values of torsion obtained from the different components, the average of the three components was calculated and saved as the average torsion. The curvature and absolute values of the average torsion were calculated for all points of the central line of the axon. Curvature and average torsion were normalized by the distance between two consecutive points on the central axon line.

4.7 | Quantifications and statistical analysis

Sample size was chosen according to previous analyses of similar parameters (Eichel et al., 2020; Erwig et al., 2019). Bar graphs in Figure 2a, b display datapoints representing biological replicates (i.e. individual mice), mean and SEM; violin plots in Figure 2a, b′ display datapoints representing all outfoldings assessed in all biological replicates, median and interquartile ranges; bar graphs in Figure 2c, d display percentage and SEM; plots in Figure 3c–f display frequency distributions; plots in Figure 4a, b display frequency distributions; bar graphs in Figure 4c, g display datapoints representing biological replicates (i.e., individual mice), mean and SEM.

Axonal curvature, torsion, eccentricity and circumference frequency in Figure 3c–f were assessed by Kolmogorov–Smirnov (KS) test. Shifts in axonal diameters between experimental groups in Figure 4a, b were assessed by Kolmogorov–Smirnov (KS) test of frequency distribution in Rstudio (www.rstudio.com, version 3.4.1) as previously described in detail (Eichel et al., 2020) available at https://github.com/MariaEichel/FrequencyDistributions. Morphological features in Figures 2a, b and 4c–g were assessed by one-tailed t-test.

Levels of significance were set at $p < .05$ (*), $p < .01$ (**), and $p < .001$ (***). Exact p-values are given in the figure legends or within in the figure (Figure 3c–f).

AUTHOR CONTRIBUTIONS

Investigation, supervision, methodology, writing-review & editing: Anna M. Steyer. *Investigation, writing-review & editing*: Tobias J. Buscham. *Investigation, methodology, writing-review & editing*: Charlotta Lorenz. *Investigation, writing-review & editing*: Sophie Hümmert. *Investigation, writing-review & editing*: Maria A. Eichel-Vogel. *Investigation, writing-review & editing*: Leonie C. Schadt. *Interpretation of data, writing-review & editing*: Julia M. Edgar. *Supervision, methodology, writing-review & editing*: Sarah Köster. *Supervision, methodology, writing-review & editing*: Wiebke Möbius. *Interpretation of data, writing-review & editing*: Klaus-Armin Nave. *Conceptualization, supervision, interpretation of data, writing-original draft, writing-review & editing*: Hauke B. Werner.

ACKNOWLEDGMENTS

We thank R. Jung, C. Sigg and T. Ruhwedel for technical support, H. Li and A. Munk for discussion, and J. Ficner for help with graphics. This work was funded by German Research Foundation (DFG) grant WE 2720/2-2 to HBW. Funding was also provided by DFG grants WE 2720/4-1 and WE 2720/5-1 to HBW, DFG grant EXC 2067/1-390729940 to SK, DFG Collaborative Research Center (SFB) 1286 'Quantitative Synaptology' project B02 to SK, European Research

10981136, 2023, 3, Downloaded from https://onlinelibrary.wiley.com/doi/10.1002/glia.24290 by University Of Glasgow, Wiley Online Library on [24/01/2023]. See the Terms and Conditions (https://onlinelibrary.wiley.com/terms-and-conditions) on Wiley Online Library for rules of use; OA articles are governed by the applicable Creative Commons License

Council (ERC) Consolidator Grant 724932 to SK, and ERC Advanced Grant MyeliNano to KAN. The funders had no role in study design, data collection and interpretation, or the decision to submit the work for publication. Open Access funding enabled and organized by Projekt DEAL.

DATA AVAILABILITY STATEMENT

The datasets analyzed in the current study have been uploaded to the Electron Microscopic Image Archive (EMPIAR); upon acceptance of this paper they will be made publicly accessible with accession numbers EMPIAR-11214, EMPIAR-11215, EMPIAR-11216, EMPIAR-11219, EMPIAR-11220, EMPIAR-11237, EMPIAR-11238, EMPIAR-11239 and EMPIAR-11240.

ORCID

Anna M. Steyer https://orcid.org/0000-0002-4814-7517
Maria A. Eichel-Vogel https://orcid.org/0000-0002-9925-7249
Julia M. Edgar https://orcid.org/0000-0002-3869-0962
Sarah Köster https://orcid.org/0000-0002-0009-1024
Wiebke Möbius https://orcid.org/0000-0002-2902-7165
Klaus-Armin Nave https://orcid.org/0000-0001-8724-9666
Hauke B. Werner https://orcid.org/0000-0002-7710-5738

REFERENCES

Adlkofer, K., Martini, R., Aguzzi, A., Zielasek, J., Toyka, K. V., & Suter, U. (1995). Hypermyelination and demyelinating peripheral neuropathy in Pmp22-deficient mice. *Nature Genetics*, *11*, 274–280.

Andersson, M., Kjer, H. M., Rafael-Patino, J., Pacureanu, A., Pakkenberg, B., Thiran, J. P., Ptito, M., Bech, M., Dahl, A. B., Dahl, V. A., & Dyrby, T. B. (2021). Axon morphology is modulated by the local environment and impacts the noninvasive investigation of its structure–function relationship. *Proceedings of the National Academy of Sciences of the United States of America*, *117*, 33649–33659.

Bakhti, M., Snaidero, N., Schneider, D., Aggarwal, S., Möbius, W., Janshoff, A., Eckhardt, M., Nave, K. A., & Simons, M. (2013). Loss of electrostatic cell-surface repulsion mediates myelin membrane adhesion and compaction in the central nervous system. *Proceedings of the National Academy of Sciences of the United States of America*, *110*, 3143–3148.

Bartsch, S., Montag, D., Schachner, M., & Bartsch, U. (1997). Increased number of unmyelinated axons in optic nerves of adult mice deficient in the myelin-associated glycoprotein (MAG). *Brain Research*, *762*, 231–234.

Belevich, I., Joensuu, M., Kumar, D., Vihinen, H., & Jokitalo, E. (2016). Microscopy image browser: A platform for segmentation and analysis of multidimensional datasets. *PLoS Biology*, *14*, 1–13.

Biffiger, K., Bartsch, S., Montag, D., Aguzzi, A., Schachner, M., & Bartasch, U. (2000). Severe hypomyelination of the murine CNS in the absence of myelin-associated glycoprotein and Fyn tyrosine kinase. *Journal of Neuroscience*, *20*, 7430–7437.

Bizzozero, O. A., Bixler, H. A., Davis, J. D., Espinosa, A., & Messier, A. M. (2001). Chemical deacylation reduces the adhesive properties of proteolipid protein and leads to decompaction of the myelin sheath. *Journal of Neurochemistry*, *76*, 1129–1141.

Boison, D., Büssow, H., D'Urso, D., Müller, H. W., & Stoffel, W. (1995). Adhesive properties of proteolipid protein are responsible for the compaction of CNS myelin sheaths. *Journal of Neuroscience*, *15*, 5502–5513.

Bowley, M. P., Cabral, H., Rosene, D. L., & Peters, A. (2010). Age changes in myelinated nerve fibers of the cingulate bundle and corpus callosum in the rhesus monkey. *Journal of Comparative Neurology*, *518*, 3046–3064.

Cailloux, F., Gauthier-Barichard, F., Mimault, C., Isabelle, V., Courtois, V., Giraud, G., … Boespflug-Tanguy, O. (2000). Genotype-phenotype correlation in inherited brain myelination defects due to proteolipid protein gene mutations. Clinical European Network on Brain Dysmyelinating Disease. *Eur J Hum Genet*, *8*, 837–845.

Costa, A. R., Pinto-Costa, R., Sousa, S. C., & Sousa, M. M. (2018). The regulation of axon diameter: From axonal circumferential contractility to activity-dependent axon swelling. *Frontiers in Molecular Neuroscience*, *11*, 319.

Costa, A. R., Sousa, S. C., Pinto-Costa, R., Mateus, J. C., Lopes, C. D. F., Costa, A. C., Rosa, D., Machado, D., Pajuelo, L., Wang, X., Zhou, F. Q., Pereira, A. J., Sampaio, P., Rubinstein, B. Y., Pinto, I. M., Lampe, M., Aguiar, P., & Sousa, M. M. (2020). The membrane periodic skeleton is an actomyosin network that regulates axonal diameter and conduction. *eLife*, *9*, e55471.

Cullen, M. J., & Webster, H. D. (1979). Remodelling of optic nerve myelin sheaths and axons during metamorphosis in Xenopus laevis. *Journal of Comparative Neurology*, *184*, 353–362.

De Monasterio-Schrader, P., Patzig, J., Möbius, W., Barrette, B., Wagner, T. L., Kusch, K., Edgar, J. M., Brophy, P. J., & Werner, H. B. (2013). Uncoupling of neuroinflammation from axonal degeneration in mice lacking the myelin protein tetraspanin-2. *Glia*, *61*, 1832–1847.

Deerinck, T. J., Bushong, E. A., Thor, A., & Ellisman, M. H. (2010). NCMIR methods for 3D EM: A new protocol for preparation of biological specimens for serial block face scanning electron microscopy. *Microscopy*, *2014*, 6–8.

Djannatian, M., Timmler, S., Arends, M., Luckner, M., Weil, M. T., Alexopoulos, I., Snaidero, N., Schmid, B., Misgeld, T., Möbius, W., Schifferer, M., Peles, E., & Simons, M. (2019). Two adhesive systems cooperatively regulate axon ensheathment and myelin growth in the CNS. *Nature Communications*, *10*, 4794.

Djannatian M, Weikert U, Safaiyan S, Wrede C, Kislinger G, Ruhwedel T, Campbell DS, van Ham T, Schmid B, Hegermann J, Möbius W, Schifferer M, Simons M. 2021. Myelin biogenesis is associated with pathological ultrastructure that is resolved by microglia during development. bioRxiv.

Duncan, G. J., Simkins, T. J., & Emery, B. (2021). Neuron-oligodendrocyte interactions in the structure and integrity of axons. *Frontiers in Cell and Developmental Biology*, *9*, 613–627.

Edgar, J., McLaughlin, M., Yool, D., Zhang, S., Fowler, J., Montague, P., Barrie, J., McCulloch, M., Duncan, I., Garbern, J., Nave, K., & Griffiths, I. (2004). Oligodendroglial modulation of fast axonal transport in a mouse model of hereditary spastic paraplegia. *The Journal of Cell Biology*, *166*, 121–131.

Eichel, M. A., Gargareta, V. I., D'Este, E., Fledrich, R., Kungl, T., Buscham, T. J., Lüders, K. A., Miracle, C., Jung, R. B., Distler, U., Kusch, K., Möbius, W., Hülsmann, S., Tenzer, S., Nave, K. A., & Werner, H. B. (2020). CMTM6 expressed on the adaxonal Schwann cell surface restricts axonal diameters in peripheral nerves. *Nature Communications*, *11*, 4514.

Elazar, N., Vainshtein, A., Rechav, K., Tsoory, M., Eshed-Eisenbach, Y., & Peles, E. (2019). Coordinated internodal and paranodal adhesion controls accurate myelination by oligodendrocytes. *Journal of Cell Biology*, *218*, 2887–2895.

Erb, M., Flueck, B., Kern, F., Erne, B., Steck, A. J., & Schaeren-Wiemers, N. (2006). Unraveling the differential expression of the two isoforms of myelin-associated glycoprotein in a mouse expressing GFP-tagged S-MAG specifically regulated and targeted into the different myelin compartments. *Molecular and Cellular Neuroscience*, *31*, 613–627.

10981136, 2023, 3, Downloaded from https://onlinelibrary.wiley.com/doi/10.1002/glia.24290 by University Of Glasgow, Wiley Online Library on [24/01/2023]. See the Terms and Conditions (https://onlinelibrary.wiley.com/terms-and-conditions) on Wiley Online Library for rules of use; OA articles are governed by the applicable Creative Commons License

Erwig, M. S., Patzig, J., Steyer, A. M., Dibaj, P., Heilmann, M., Heilmann, I., Jung, R. B., Kusch, K., Möbius, W., Jahn, O., Nave, K.-A., & Werner, H. B. (2019). Anillin facilitates septin assembly to prevent pathological outfoldings of central nervous system myelin. *eLife*, *8*, e43888.

Garbern, J. Y., Yool, D. A., Moore, G. J., Wilds, I. B., Faulk, M. W., Klugmann, M., Nave, K. A., Sistermans, E. A., Van Der Knaap, M. S., Bird, T. D., Shy, M. E., Kamholz, J. A., & Griffiths, I. R. (2002). Patients lacking the major CNS myelin protein, proteolipid protein 1, develop length-dependent axonal degeneration in the absence of demyelination and inflammation. *Brain*, *125*, 551–561.

Gargareta, V., Reuschenbach, J., Siems, S. B., Sun, T., Piepkorn, L., Mangana, C., Späte, E., Goebbels, S., Huitinga, I., Möbius, W., Nave, K.-A., Jahn, O., & Werner, H. B. (2022). Conservation and divergence of myelin proteome and oligodendrocyte transcriptome profiles between humans and mice. *eLife*, *11*, e77019.

Giacci, M. K., Bartlett, C. A., Huynh, M., Kilburn, M. R., Dunlop, S. A., & Fitzgerald, M. (2018). Three dimensional electron microscopy reveals changing axonal and myelin morphology along normal and partially injured optic nerves. *Scientific Reports*, *8*, 3979.

Goebbels, S., Oltrogge, J. H., Wolfer, S., Wieser, G. L., Nientiedt, T., Pieper, A., Ruhwedel, T., Groszer, M., Sereda, M. W., & Nave, K. A. (2012). Genetic disruption of Pten in a novel mouse model of tomaculous neuropathy. *EMBO Molecular Medicine*, *4*, 486–499.

Golan, N., Kartvelishvily, E., Spiegel, I., Salomon, D., Sabanay, H., Rechav, K., Vainshtein, A., Frechter, S., Maik-Rachline, G., Eshed-Eisenbach, Y., Momoi, T., & Peles, E. (2013). Genetic deletion of Cadm4 results in myelin abnormalities resembling Charcot-Marie-tooth neuropathy. *Journal of Neuroscience*, *33*, 10950–10961.

Gould, E. A., Busquet, N., Shepherd, D., Dietz, R. M., Herson, P. S., De Souza, F. M. S., Li, A., George, N. M., Restrepo, D., & Macklin, W. B. (2018). Mild myelin disruption elicits early alteration in behavior and proliferation in the subventricular zone. *eLife*, *7*, E34783.

Griffiths, I., Klugmann, M., Anderson, T., Yool, D., Thomson, C., Schwab, M. H., Schneider, A., Zimmermann, F., McCulloch, M., Nadon, N., & Nave, K. A. (1998). Axonal swellings and degeneration in mice lacking the major proteolipid of myelin. *Science*, *280*, 1610–1613.

Hartline, D. K., & Colman, D. R. (2007). Rapid conduction and the evolution of Giant axons and myelinated fibers. *Current Biology*, *17*, R29–R35.

Hill, R. A., Li, A. M., & Grutzendler, J. (2018). Lifelong cortical myelin plasticity and age-related degeneration in the live mammalian brain. *Nature Neuroscience*, *21*, 683–695.

Horn, M., Baumann, R., Pereira, J. A., Sidiropoulos, P. N. M., Somandin, C., Welzl, H., Stendel, C., Lühmann, T., Wessig, C., Toyka, K. V., Relvas, J. B., Senderek, J., & Suter, U. (2012). Myelin is dependent on the Charcot-Marie-tooth type 4H disease culprit protein FRABIN/FGD4 in Schwann cells. *Brain*, *135*, 3567–3583.

Hu, B., Arpag, S., Zhang, X., Möbius, W., Werner, H., Sosinsky, G., Ellisman, M., Zhang, Y., Hamilton, A., Chernoff, J., & Li, J. (2016). Tuning PAK activity to rescue abnormal myelin permeability in HNPP. *PLoS Genetics*, *12*, E1006290.

Inoue, K. (2019). Pelizaeus-Merzbacher disease: Molecular and cellular pathologies and associated phenotypes. *Adv Exp Med Biol*, *1190*, 201–216.

Jahn, O., Siems, S. B., Kusch, K., Hesse, D., Jung, R. B., Liepold, T., Uecker, M., Sun, T., & Werner, H. B. (2020). The CNS myelin proteome: Deep profile and persistence after post-mortem delay. *Frontiers in Cellular Neuroscience*, *14*, 239.

Kammers, K., Cole, R. N., Tiengwe, C., & Ruczinski, I. (2015). Detecting significant changes in protein abundance. *EuPA Open Proteomics*, *7*, 11–19.

Katanov, C., Novak, N., Vainshtein, A., Golani, O., Dupree, J. L., & Peles, E. (2020). N-wasp regulates oligodendrocyte myelination. *Journal of Neuroscience*, *40*, 6103–6111.

Kim, S., Maynard, J. C., Sasaki, Y., Strickland, A., Sherman, D. L., Brophy, P. J., Burlingame, A. L., & Milbrandt, J. (2016). Schwann cell O-GlcNAc glycosylation is required for myelin maintenance and axon integrity. *Journal of Neuroscience*, *36*, 9633–9646.

Kinter, J., Lazzati, T., Schmid, D., Zeis, T., Erne, B., Lützelschwab, R., Steck, A. J., Pareyson, D., Peles, E., & Schaeren-Wiemers, N. (2013). An essential role of MAG in mediating axon-myelin attachment in Charcot-Marie-tooth 1A disease. *Neurobiology of Disease*, *49*, 221–231.

Klugmann, M., Schwab, M. H., Pühlhofer, A., Schneider, A., Zimmermann, F., Griffiths, I. R., & Nave, K. A. (1997). Assembly of CNS myelin in the absence of proteolipid protein. *Neuron*, *18*, 59–70.

Lappe-Siefke, C., Goebbels, S., Gravel, M., Nicksch, E., Lee, J., Braun, P. E., Griffiths, I. R., & Nave, K. A. (2003). Disruption of Cnp1 uncouples oligodendroglial functions in axonal support and myelination. *Nature Genetics.*, *33*, 366–374.

Lee, J. K., Geoffroy, C. G., Chan, A. F., Tolentino, K. E., Crawford, M. J., Leal, M. A., Kang, B., & Zheng, B. (2010). Assessing spinal axon regeneration and sprouting in Nogo-, MAG-, and OMgp-deficient mice. *Neuron*, *66*, 663–670.

Leite, S. C., Sampaio, P., Sousa, V. F., Nogueira-Rodrigues, J., Pinto-Costa, R., Peters, L. L., Brites, P., & Sousa, M. M. (2016). The Actin-binding protein α-Adducin is required for maintaining axon diameter. *Cell Reports*, *15*, 490–498.

Li, C., Trapp, B., Ludwin, S., Peterson, A., & Roder, J. (1998). Myelin associated glycoprotein modulates glia-axon contact in vivo. *Journal of Neuroscience Research*, *51*, 210–217.

Li, C., Tropak, M. B., Gerlai, R., Clapoff, S., Abramow-Newerly, W., Trapp, B., Peterson, A., & Roder, J. (1994). Myelination in the absence of myelin-associated glycoprotein. *Nature*, *369*, 747–750.

Li, S., Liu, B. P., Budel, S., Li, M., Ji, B., Walus, L., Li, W., Jirik, A., Rabacchi, S., Choi, E., Worley, D., Sah, D. W. Y., Pepinsky, B., Lee, D., Relton, J., & Strittmatter, S. M. (2004). Blockade of Nogo-66, myelin-associated glycoprotein, and oligodendrocyte myelin glycoprotein by soluble Nogo-66 receptor promotes axonal sprouting and recovery after spinal injury. *Journal of Neuroscience*, *24*, 10511–10520.

Liu, B. P., Fournier, A., GrandPré, T., & Strittmatter, S. M. (2002). Myelin-associated glycoprotein as a functional ligand for the Nogo-66 receptor. *Science*, *297*, 1190–1193.

Lossos, A., Ponger, P., Newman, J. P., Elazar, N., Mor, N., Eshed-Eisenbach, Y., Peles, E., Lerer, I., B.-E. Z., Marreed, H., Meiner, V., Schueler-Furman, O., Fellig, Y., Azulay, H., Glick, B., Dotan, S., Goldberg, S., Gomori, J. M., Steck, A. J., … Geiger, T. (2015). Myelin-associated glycoprotein gene mutation causes Pelizaeus-Merzbacher disease-like disorder. *Brain*, *138*, 2521–2536.

Lüders, K. A., Nessler, S., Kusch, K., Patzig, J., Jung, R. B., Möbius, W., Nave, K. A., & Werner, H. B. (2019). Maintenance of high proteolipid protein level in adult central nervous system myelin is required to preserve the integrity of myelin and axons. *Glia*, *67*, 634–649.

Lüders, K. A., Patzig, J., Simons, M., Nave, K. A., & Werner, H. B. (2017). Genetic dissection of oligodendroglial and neuronal Plp1 function in a novel mouse model of spastic paraplegia type 2. *Glia*, *65*, 1762–1776.

Marcus, J., Dupree, J., & Popko, B. (2002). Myelin-associated glycoprotein and myelin galactolipids stabilize developing axo-glial interactions. *The Journal of Cell Biology*, *156*, 567–577.

McKerracher, L., David, S., Jackson, D. L., Kottis, V., Dunn, R. J., & Braun, P. E. (1994). Identification of myelin-associated glycoprotein as a major myelin-derived inhibitor of neurite growth. *Neuron*, *13*, 805–811.

McKerracher, L., & Rosen, K. M. (2015). MAG, myelin and overcoming growth inhibition in the CNS. *Frontiers in Molecular Neuroscience*, *8*, 51.

Möbius, W., Patzig, J., Nave, K. A., & Werner, H. B. (2008). Phylogeny of proteolipid proteins: Divergence, constraints, and the evolution of novel functions in myelination and neuroprotection. *Neuron Glia Biology*, *4*, 111–127.

Montag, D., Giese, K. P., Bartsch, U., Martini, R., Lang, Y., Blüthmann, H., Karthigasan, J., Kirschner, D. A., Wintergerst, E. S., Nave, K.-A.,

10981136, 2023, 3, Downloaded from https://onlinelibrary.wiley.com/doi/10.1002/glia.24290 by University Of Glasgow, Wiley Online Library on [24/01/2023]. See the Terms and Conditions (https://onlinelibrary.wiley.com/terms-and-conditions) on Wiley Online Library for rules of use; OA articles are governed by the applicable Creative Commons License

Zielasek, J., Toyka, K. V., Lipp, H.-P., & Schachner, M. (1994). Mice deficient for the glycoprotein show subtle abnormalities in myelin. *Neuron*, *13*, 229–246.

Mukhopadhyay, G., Doherty, P., Walsh, F. S., Crocker, P. R., & Filbin, M. T. (1994). A novel role for myelin-associated glycoprotein as an inhibitor of axonal regeneration. *Neuron*, *13*, 757–767.

Myllykoski, M., Eichel, M. A., Jung, R. B., Kelm, S., Werner, H. B., & Kursula, P. (2018). High-affinity heterotetramer formation between the large myelin-associated glycoprotein and the dynein light chain DYNLL1. *Journal of Neurochemistry*, *147*, 764–783.

Nave, K., & Werner, H. (2021). Ensheathment and myelination of axons: Evolution of glial functions. *Annual Review of Neuroscience*, *44*, 197–219.

Nave, K.-A., & Werner, H. B. (2014). Myelination of the nervous system: Mechanisms and functions. *Annual Review of Cell and Developmental Biology*, *30*, 503–533.

Nguyen, T., Mehta, N. R., Conant, K., Kim, K. J., Jones, M., Calabresi, P. A., Melli, G., Hoke, A., Schnaar, R. L., Ming, G. L., Song, H., Keswani, S. C., & Griffin, J. W. (2009). Axonal protective effects of the myelin-associated glycoprotein. *Journal of Neuroscience*, *29*, 630–637.

Novarino, G., Fenstermaker, A. G., Zaki, M. S., Hofree, M., Silhavy, J. L., Heiberg, A. D., Abdellateef, M., Rosti, B., Scott, E., Mansour, L., Masri, A., Kayserili, H., Al-Aama, J. Y., Abdel-Salam, G. M. H., Karminejad, A., Kara, M., Kara, B., Bozorgmehri, B., Ben-Omran, T., … Gleeson, J. G. (2014). Exome sequencing links corticospinal motor neuron disease to common neurodegenerative disorders. *Science*, *343*, 506–511.

Pan, B., Fromholt, S. E., Hess, E. J., Crawford, T. O., Griffin, J. W., Sheikh, K. A., & Schnaar, R. L. (2005). Myelin-associated glycoprotein and complementary axonal ligands, gangliosides, mediate axon stability in the CNS and PNS: Neuropathology and behavioral deficits in single- and double-null mice. *Experimental Neurology*, *195*, 208–217.

Pernet, V., Joly, S., Christ, F., Dimou, L., & ME, S. (2008). Nogo-A and myelin-associated glycoprotein differently regulate oligodendrocyte maturation and myelin formation. *J Neurosci*, *28*, 7435–7444.

Patzig, J., Erwig, M. S., Tenzer, S., Kusch, K., Dibaj, P., Möbius, W., Goebbels, S., Schaeren-Wiemers, N., Nave, K. A., & Werner, H. B. (2016). Septin/anillin filaments scaffold central nervous system myelin to accelerate nerve conduction. *eLife*, *5*, e17119.

Patzig, J., Kusch, K., Fledrich, R., Eichel, M. A., Lüders, K. A., Möbius, W., Sereda, M. W., Nave, K.-A., Martini, R., & Werner, H. B. (2016). Proteolipid protein modulates preservation of peripheral axons and premature death when myelin protein zero is lacking. *Glia*, *64*, 155–174.

Peters, A. (2002). The effects of normal aging on myelin and nerve fibers: A review. *Journal of Neurocytology*, *31*, 581–593.

Philips, T., & Rothstein, J. D. (2017). Oligodendroglia: Metabolic supporters of neurons. *The Journal of Clinical Investigation*, *127*, 3271–3280.

Rosenbluth, J. (1966). Redundant myelin sheaths and other ultrastructural features of the toad cerebellum. *The Journal of Cell Biology*, *28*, 73–93.

Roubertie ,A., Charif, M., Meyer, P., Manes, G., Meunier, I., Taieb, G., Junta Morales, R., … Lenaers, G. (2019). Hereditary spastic paraplegia and prominent sensorial involvement: Think MAG mutations! *Ann Clin Transl Neurol*, *6*, 1572–1577.

Saugier-Veber, P., Munnich, A., Bonneau, D., Rozet, J. M., le Merrer, M., Gil, R., Boespflug-Tanguy, O. (1994). X-linked spastic paraplegia and Pelizaeus-Merzbacher disease are allelic disorders at the proteolipid protein locus. *Nature Genetics*, *6*, 257-262.

Schindelin, J., Arganda-Carreras, I., Frise, E., Kaynig, V., Longair, M., Pietzsch, T., Preibisch, S., Rueden, C., Saalfeld, S., Schmid, B., Tinevez, J. Y., White, D. J., Hartenstein, V., Eliceiri, K., Tomancak, P., & Cardona, A. (2012). Fiji: An open-source platform for biological-image analysis. *Nature Methods*, *9*, 676–682.

Shen, Y. J., DeBellard, M. E., Salzer, J. L., Roder, J., & Filbin, M. T. (1998). Myelin-associated glycoprotein in myelin and expressed by Schwann cells inhibits axonal regeneration and branching. *Molecular and Cellular Neurosciences*, *12*, 79–91.

Sicotte, M., Tsatas, O., Jeong, S. Y., Cai, C. Q., He, Z., & David, S. (2003). Immunization with myelin or recombinant Nogo-66/MAG in alum promotes axon regeneration and sprouting after corticospinal tract lesions in the spinal cord. *Molecular and Cellular Neuroscience*, *23*, 251–263.

Siems, S. B., Jahn, O., Eichel, M. A., Kannaiyan, N., Wu, L. M. N., Sherman, D. L., Kusch, K., Hesse, D., Jung, R. B., Fledrich, R., Sereda, M. W., Rossner, M. J., Brophy, P. J., & Werner, H. B. (2020). Proteome profile of peripheral myelin in healthy mice and in a neuropathy model. *eLife*, *9*, e51406.

Sinoway, M. P., Kitagawa, K., Timsit, S., Hashim, G. A., Hashim, G. A., & Colman, D. R. (1994). Proteolipid protein interactions in transfectants: Implications for myelin assembly. *Journal of Neuroscience Research*, *37*, 551–562.

Snaidero, N., Möbius, W., Czopka, T., Hekking, L. H. P., Mathisen, C., Verkleij, D., Goebbels, S., Edgar, J., Merkler, D., Lyons, D. A., Nave, K. A., & Simons, M. (2014). Myelin membrane wrapping of CNS axons by PI(3,4,5)P3-dependent polarized growth at the inner tongue. *Cell*, *156*, 277–290.

Sommer, C., Straehle, C., Koethe, U., & Hamprecht, F. A. (2011). Ilastik: Interactive learning and segmentation toolkit. *iEEE International Symposium on Biomedical Imaging (ISBI)*, 230–233.

Stadelmann, C., Timmler, S., Barrantes-Freer, A., & Simons, M. (2019). Myelin in the central nervous system: Structure, function, and pathology. *Physiological Reviews*, *99*, 1381–1431.

Sternberg, S. (2012). *Curvature in mathematics and physics*. Dover Publications.

Steyer, A. M., Ruhwedel, T., Nardis, C., Werner, H. B., Nave, K. A., & Möbius, W. (2020). Pathology of myelinated axons in the PLP-deficient mouse model of spastic paraplegia type 2 revealed by volume imaging using focused ion beam-scanning electron microscopy. *Journal of Structural Biology*, *210*, 107492.

Sturrock, R. R. (1976). Changes in neuroglia and myelination in the white matter of aging mice. *Journals of Gerontology*, *31*, 513–522.

Trapp, B. D., & Quarles, R. H. (1984). Immunocytochemical localization of the myelin-associated glycoprotein fact or artifact? *Journal of Neuroimmunology*, *6*, 231–249.

Trevisiol, A., Kusch, K., Steyer, A. M., Gregor, I., Nardis, C., Winkler, U., Köhler, S., Restrepo, A., Möbius, W., Werner, H. B., Nave, K. A., & Hirrlinger, J. (2020). Structural myelin defects are associated with low axonal ATP levels but rapid recovery from energy deprivation in a mouse model of spastic paraplegia. *PLoS Biology*, *18*, e3000943.

Weil, M.-T., Heibeck, S., Töpperwien, M., Tom Dieck, S., Ruhwedel, T., Salditt, T., Rodicio, M. C., Morgan, J. R., Nave, K.-A., Möbius, W., & Werner, H. B. (2018). Axonal Ensheathment in the nervous system of lamprey: Implications for the evolution of Myelinating glia. *The Journal of Neuroscience*, *38*, 6586–6596.

Wolf, N. I., Ffrench-Constant, C., & van der Knaap, M. S. (2020). Hypomyelinating leukodystrophies — Unravelling myelin biology. *Nature Reviews Neurology*, *17*, 88–103.

Yin, X., Crawford, T. O., Griffin, J. W., Tu, P. H., Lee, V. M. Y., Li, C., Roder, J., & Trapp, B. D. (1998). Myelin-associated glycoprotein is a myelin signal that modulates the caliber of myelinated axons. *Journal of Neuroscience*, *18*, 1953–1962.

Yool, D. A., Klugmann, M., McLaughlin, M., Vouyiouklis, D. A., Dimou, L., Barrie, J. A., McCulloch, M. C., Nave, K. A., & Griffiths, I. R. (2001). Myelin proteolipid proteins promote the interaction of oligodendrocytes and axons. *Journal of Neuroscience Research*, *63*, 151–164.

Zech, M., Brunet, T., Škorvánek, M., Blaschek, A., Vill, K., Hanker, B., … Winkelmann, J. (2020). Recessive null-allele variants in MAG

10981136, 2023, 3, Downloaded from https://onlinelibrary.wiley.com/doi/10.1002/glia.24290 by University Of Glasgow, Wiley Online Library on [24/01/2023]. See the Terms and Conditions (https://onlinelibrary.wiley.com/terms-and-conditions) on Wiley Online Library for rules of use; OA articles are governed by the applicable Creative Commons License

associated with spastic ataxia, nystagmus, neuropathy, and dystonia. *Parkinsonism Relat Disord*, *77*, 70–75.

SUPPORTING INFORMATION

Additional supporting information can be found online in the Supporting Information section at the end of this article.

How to cite this article: Steyer, A. M., Buscham, T. J., Lorenz, C., Hümmert, S., Eichel-Vogel, M. A., Schadt, L. C., Edgar, J. M., Köster, S., Möbius, W., Nave, K.-A., & Werner, H. B. (2023). Focused ion beam-scanning electron microscopy links pathological myelin outfoldings to axonal changes in mice lacking *Plp1* or *Mag*. *Glia*, *71*(3), 509–523. https://doi.org/10.1002/glia.24290

10981136, 2023, 3, Downloaded from https://onlinelibrary.wiley.com/doi/10.1002/glia.24290 by University Of Glasgow, Wiley Online Library on [24/01/2023]. See the Terms and Conditions (https://onlinelibrary.wiley.com/terms-and-conditions) on Wiley Online Library for rules of use; OA articles are governed by the applicable Creative Commons License